

High-throughput microplastic screening system using multispectral fluorescence imaging under UV excitation

Asuka Sawamoto^a and Shigeki Nakauchi^b

^{a,b}Department of Computer Science and Engineering, Toyohashi University of Technology, 1-1 Hibarigaoka, Tempaku-cho, Toyohashi, Aichi, Japan 441-8580

ABSTRACT

The widespread contamination of microplastics (MPs) necessitates comprehensive monitoring across various environments. However, standard analytical methods, such as FTIR and Raman spectroscopy, rely on point-scanning, which is time-consuming and resource-intensive, limiting their utility for high-throughput screening. Here, we propose a rapid multispectral imaging method using polymer auto-fluorescence under UV excitation. Leveraging the distinct fingerprints observed in Excitation-Emission Matrices (EEMs), our approach optimizes spectral acquisition by selecting a minimal subset of effective spectral bands rather than measuring the full sets of spectra in the EEM. Using a Random Forest-based feature selection, we demonstrated that a subset of 5 spectral bands maximizes the classification performance for 9 representative virgin polymers, achieving a weighted F1-score of 0.92. This significant reduction in spectral dimensionality enables the design of simplified hardware using commercially available UV-LEDs, offering a practical and accessible solution for high-throughput MP monitoring.

Keywords: Microplastics, Multispectral fluorescence imaging, UV excitation, High-throughput screening, Spectral optimization, Excitation-emission matrix

1. INTRODUCTION

The widespread accumulation of microplastics (MPs) in the natural environment is an increasingly serious global issue [1, 2]. Understanding MP pollution sources and dynamics requires comprehensively quantifying their distribution and flux across various media [3]. Specifically, tracking pollution sources and environmental behavior, identifying the specific material type, such as polyethylene (PE) from packaging vs. polyethylene terephthalate (PET) from bottles, of every single sample collected in field surveys is essential [4].

However, while conventional analytical methods such as Fourier Transform Infrared Spectroscopy (FTIR) and Raman spectroscopy excel at identifying the chemical structure of MPs, they rely on point-scanning, which requires an enormous amount of time for analysis [5, 6]. Such techniques typically utilize bulky, expensive instrumentation restricted to laboratory settings, limiting mobility for on-site monitoring [5]. Comprehensive chemical profiling of the vast amounts of MPs in the environment is virtually impossible within a realistic timeframe. In-process applications demand high-throughput solutions achieving both practical classification accuracy and rapid analysis speeds [7]. To address this need, hyperspectral imaging (HSI) has emerged as a high-throughput alternative. Recently, Gebejes et al. demonstrated the successful identification of irregular-shaped microplastics directly in water using short-wave infrared (SWIR) HSI, overcoming water absorption interference through advanced signal processing [8].

Excitation-Emission Matrix (EEM) spectroscopy enables the non-destructive characterization of chemical compositions. When coupled with supervised machine learning algorithms, it facilitates the robust classification of complex environmental samples [9]. The diagnostic potential of fluorescence excitation scanning has notably been demonstrated in the medical field; for instance, Leavesley et al. applied hyperspectral imaging of fluorescence excitation spectra to successfully discriminate between normal and cancerous colorectal tissues [10]. Building on this versatility, our research group has previously extended this approach to fluorescence imaging to visualize

Further author information: (Send correspondence to A.S.)

A.S.: E-mail: sawamoto.asuka.us@tut.jp, Telephone: +81 90 7647 0330

the spatial distribution of quality attributes. Specifically, we successfully visualized the distribution of freshness indices (such as K-value and IMP content) in frozen fish fillets [11] and achieved non-destructive prediction of pH in frozen fish meat [12].

In the context of MP monitoring, Maes et al. established a rapid screening approach using fluorescent tagging with Nile Red [13]. More recently, Li et al. proposed a fluorescence polarimetry method to identify plastic types [14]. While these approaches are effective, a label-free method utilizing intrinsic auto-fluorescence is more desirable for in-process monitoring to eliminate sample preparation steps.

Specifically, the combination of fluorescence spectroscopy and machine learning has been established as a powerful tool for rapid classification tasks in food quality assessment. Successful applications have been widely reported, ranging from the monitoring of fish and meat products [15] and classification of olive oils [16] to the automated detection of contamination on meat surfaces using deep learning [17].

Furthermore, it is well documented that selecting optimal spectral bands, rather than utilizing the full spectrum, directly contributes to system cost reduction and processing efficiency [18, 19]. For instance, Bolton et al. developed a low-cost portable system using discrete LEDs, achieving spectral performance comparable to expensive spectrometers [18]. Additionally, Mathews demonstrated that simultaneous acquisition of multiple bands effectively suppresses motion artifacts, which is critical for on-site dynamic measurements [19]. This optimization strategy facilitates the transition from bulky laboratory equipment to practical, portable hardware implementations suitable for on-site inspection [20].

In this study, we propose a multispectral imaging method specialized for polymer identification based on the EEM. By utilizing inherent polymer auto-fluorescence under UV excitation, we capture essential spectral features as images. The validity of this UV-excitation approach is supported by Jeon et al., who demonstrated successful classification of MPs using deep-UV excitation at 266 nm [21]. Moreover, Chatterjee et al. elucidated the emission mechanism of non-conjugated polymers, such as PE and PP, attributing it to space conjugation and clustering effects [22]. As a first step, toward the future construction of a high-throughput system, we conducted a feasibility study using a benchtop system equipped with a broadband light source. This study successfully identified a combination of spectral bands that minimizes measurement time while maintaining classification accuracy.

2. PRINCIPLE

2.1 Fluorescence Characteristics

Most petroleum-based synthetic polymers emit specific auto-fluorescence under ultraviolet (UV) excitation due to their chemical structures, such as electron conjugated systems, and additives [23]. This fluorescence characteristic depends on the Excitation-Emission Matrix (EEM) and serves as a unique fingerprint for each polymer type. The proposed method leverages these EEM characteristics as the physical basis for MP classification. Generally, the fluorescence intensity F at an excitation wavelength λ_{ex} and an emission wavelength λ_{em} is described by the following simplified model:

$$F(\lambda_{ex}, \lambda_{em}) = K \cdot I_0(\lambda_{ex}) \cdot (1 - 10^{-\varepsilon(\lambda_{ex})cL}) \cdot \Phi(\lambda_{ex}, \lambda_{em}), \quad (1)$$

where K is the instrument constant (geometric factors and detection efficiency), I_0 is the excitation light intensity, ε is the molar absorption coefficient, c is the concentration, L is the optical path length, and Φ is the fluorescence quantum yield. Under the dilute solution or thin film approximation, Equation (1) becomes linear with respect to the material-intrinsic parameters ε and Φ . Since the spectral profiles of ε (absorption characteristics) and Φ (emission efficiency) differ depending on the polymer type, measuring these at multiple wavelengths enables material identification.

As a preliminary experiment, we measured the EEMs of the nine target polymers (HDPE, LDPE, PP, PS, PVC, PC, PMMA, PET, and ABS) using a fluorescence spectrophotometer (F-7000, Hitachi High-Technologies Corp.). Fig. 1 shows the measured EEMs. These results confirmed that each polymer possesses a specific fluorescence spectrum under UV excitation.

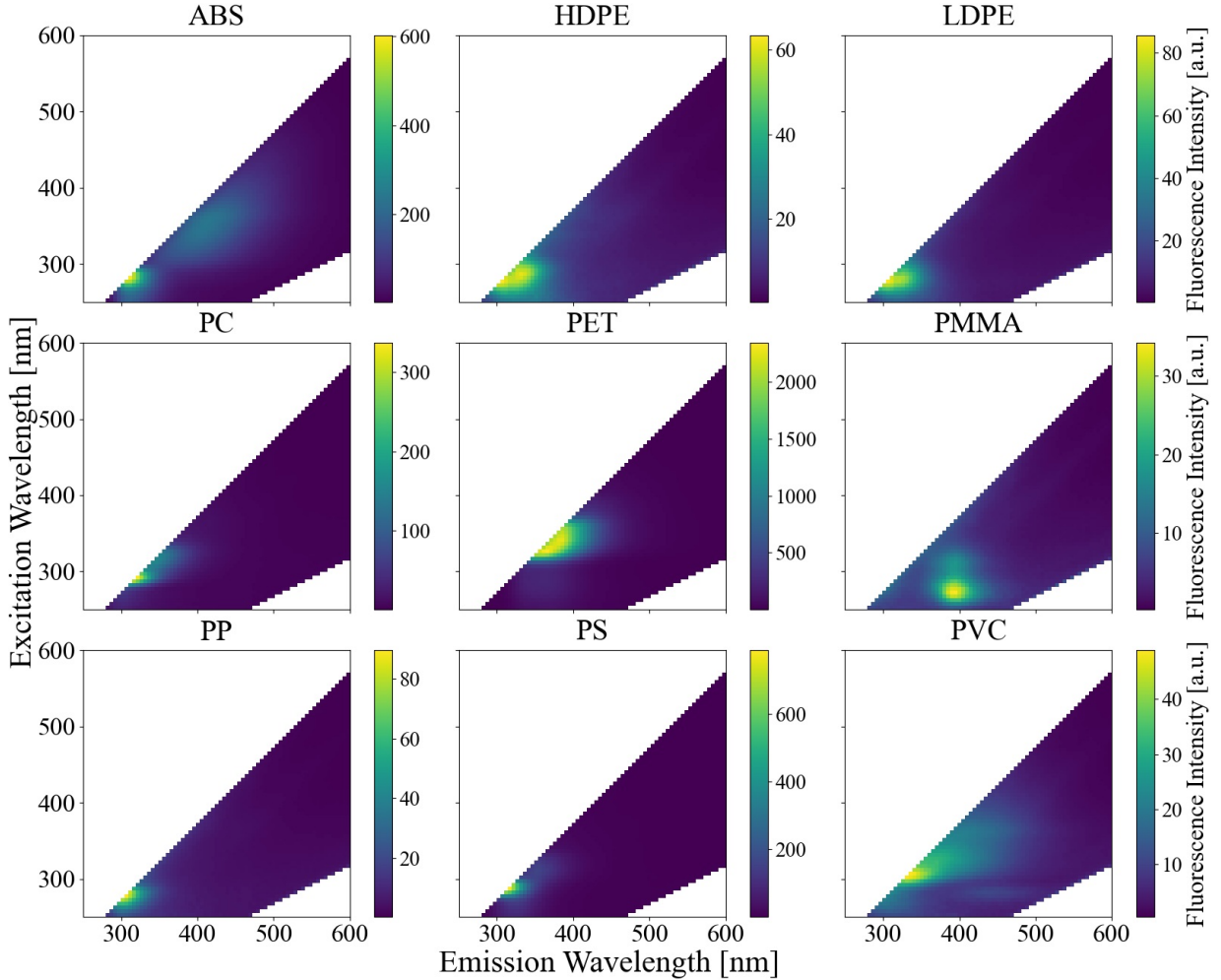


Figure 1: Measured Excitation-Emission Matrices (EEMs) of the nine types of virgin polymer pellets. The contour plots represent the fluorescence intensity [a.u.] at excitation (y-axis) and emission (x-axis) wavelengths [nm] for each polymer sample. The distinct spectral patterns (fingerprints) observed for each polymer type demonstrate the feasibility of the proposed classification method based on UV-excited fluorescence. Note: The diagonal regions corresponding to Rayleigh and Raman scattering have been computationally removed to enhance the visibility of fluorescence features.

2.2 Data-Driven Band Selection

While high-dimensional data such as EEMs are essential for accurate polymer classification, acquiring and processing the full hyperspectral datacube is inefficient for real-time applications due to the massive data volume and spectral redundancy. To address this, we require an approach to selectively acquire only the minimal spectral bands that have a high contribution to discrimination. However, since spectral data possess strong correlations between bands and contain non-linear relationships, it is difficult to determine the optimal subset using simple linear models. We used Random Forest (RF), which can account for non-linear interactions between features. In RF, the importance (Gini Importance) of a feature (spectral bands) X_j is defined as the sum of the decrease in impurity at the nodes where that feature was used for splitting, as shown in the following equation:

$$I_G(X_j) = \frac{1}{N_T} \sum_T \sum_{t \in T: v(s_t) = X_j} p(t) \Delta i(s_t, t), \quad (2)$$

where N_T is the total number of trees constituting the forest, $v(s_t)$ is the variable used for splitting at node t , $p(t)$ is the proportion of samples reaching node t , and $\Delta i(s_t, t)$ indicates the Gini Impurity Decrease due to the

split. Based on this $I_G(X_j)$, we applied a step-wise method in which bands with high importance are sequentially added and evaluated. This allowed us to determine the optimal band configuration that minimizes imaging time while maintaining classification accuracy.

3. EXPERIMENTAL SETUP

3.1 Optical Configuration

To acquire comprehensive data for spectral optimization, we used a benchtop evaluation system equipped with a broadband light source [11]. Fig. 2 shows the schematic diagram of the experimental apparatus. We used a tunable light source (MAX-303, Asahi Spectra Co., Ltd.) equipped with a broadband xenon lamp. We selected the excitation wavelength via a rotating filter wheel and guided it to the sample through an optical fiber. The fluorescence emitted from the sample passed through an emission-side bandpass filter to remove scattered excitation light, and a UV-sensitive camera (BU-56DUV, BITRAN Corp.) captured the signal.

To construct a comprehensive hyperspectral dataset, we combined excitation bandpass filters (center wavelengths: 260–380 nm) and emission bandpass filters (280–600 nm) at 20 nm intervals. By selecting valid combinations satisfying the Stokes shift (fluorescence wavelength > excitation wavelength), we acquired a total of 98 spectral images.

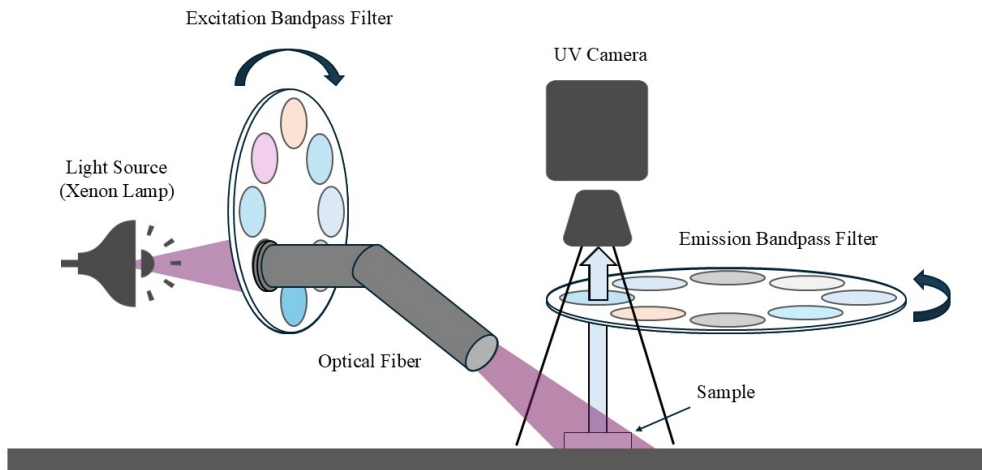


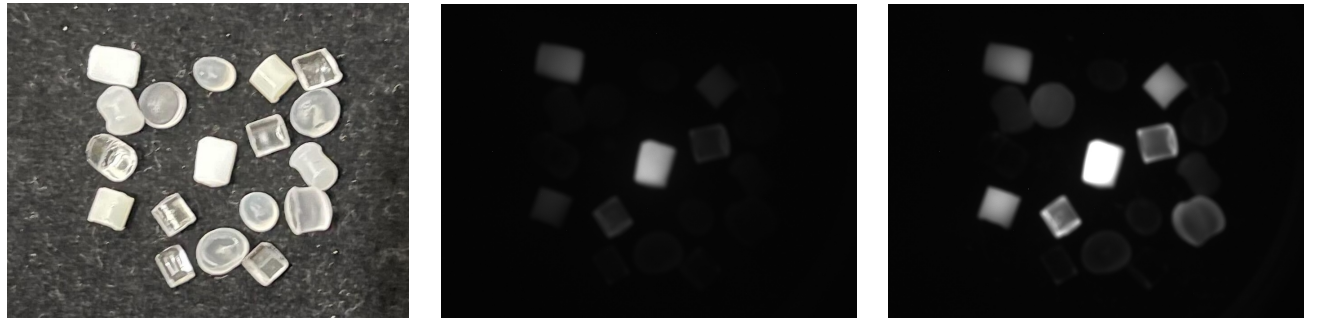
Figure 2: Schematic diagram of the benchtop evaluation system used for hyperspectral fluorescent image acquisition. A broadband xenon lamp and interchangeable bandpass filters were used to excite the samples, and the emitted fluorescence was captured by a UV-sensitive camera to construct a comprehensive dataset for spectral optimization.

3.2 Samples and Data Acquisition

We used nine types of virgin polymer pellets (HDPE, LDPE, PP, PS, PVC, PC, PMMA, PET, and ABS), which account for the majority of global plastic production, as experimental samples. The size of each pellet is approximately 3–5 mm (Fig. 3(a)). While these are transparent or white under visible light and difficult to distinguish its types, they exhibit characteristic fluorescence intensity differences under UV excitation (Fig. 3(b), (c)). To improve data acquisition efficiency, we arranged the nine types of pellets within the same field of view during imaging. We acquired the datasets used for model calibration and evaluation in independent imaging sessions with different geometric arrangements:

- **Calibration Set:** To cover spectral variations depending on the arrangement state and construct a robust model, we integrated images acquired in the following two configurations:

- **External Validation Set:** A dataset used solely for the final performance evaluation of the model, independent of the calibration process. It consists only of images with the *Dispersed Arrangement*. This verified the pure identification capability for unknown data.



(a) Visible Light **(b) Ex 320 / Em 400** **(c) Ex 360 / Em 480**

Figure 3: Images of the experimental samples consisting of nine types of virgin polymer pellets. (a) Visible light image; most samples appear transparent or white. (b, c) Representative fluorescence images acquired at (b) Ex 320 nm / Em 400 nm and (c) Ex 360 nm / Em 480 nm. Note: The sample arrangement differs between visible and fluorescence images. Despite the random arrangement, we clearly observe characteristic fluorescence intensity differences.

4. METHOD

We propose a framework for high-throughput and accurate identification by selecting optimal wavelengths from acquired hyperspectral data. The process consists of three main stages: (1) Problem Formulation, (2) Pre-processing, and (3) Feature Selection.

4.1 Problem Formulation

Let the spectral intensity vector at each pixel be $\mathbf{x} \in \mathbb{R}^D$ (where $D = 98$ corresponds to the number of acquired spectral images described in Section 3.1). Let the class label of the target polymer be $y \in \{C_1, \dots, C_9\}$. The objective of this study is to learn a mapping function $f : \mathbf{x} \rightarrow y$ that predicts the ground-truth label y from the input \mathbf{x} .

To verify the effectiveness of the proposed method, we define two experimental settings:

- **Full-Spectrum (Baseline):** A model that uses the entire wavelength band ($D = 98$) as input features. This serves as the theoretical upper limit of accuracy.
 - **Optimized-Band (Ours):** A model that uses only k important bands selected by the algorithm described below ($k \ll 98$).

4.2 Pre-processing

The pixel intensity of the acquired fluorescence images strongly depends on the geometric shape of the sample, the distance from the light source, and the non-uniformity of illumination. These intensity variations hinder accurate polymer identification. To achieve robust identification based solely on the polymer-specific spectral profile rather than absolute intensity, we applied Minimum Value Subtraction and L2 Normalization to the spectral data vector \mathbf{x} of each pixel:

$$\mathbf{x}' = \frac{\mathbf{x} - \min(\mathbf{x})}{\|\mathbf{x} - \min(\mathbf{x})\|_2}. \quad (3)$$

This process generates a normalized feature vector \mathbf{x}' that is independent of lighting conditions and sample arrangement.

4.3 Spectral Feature Selection Strategy

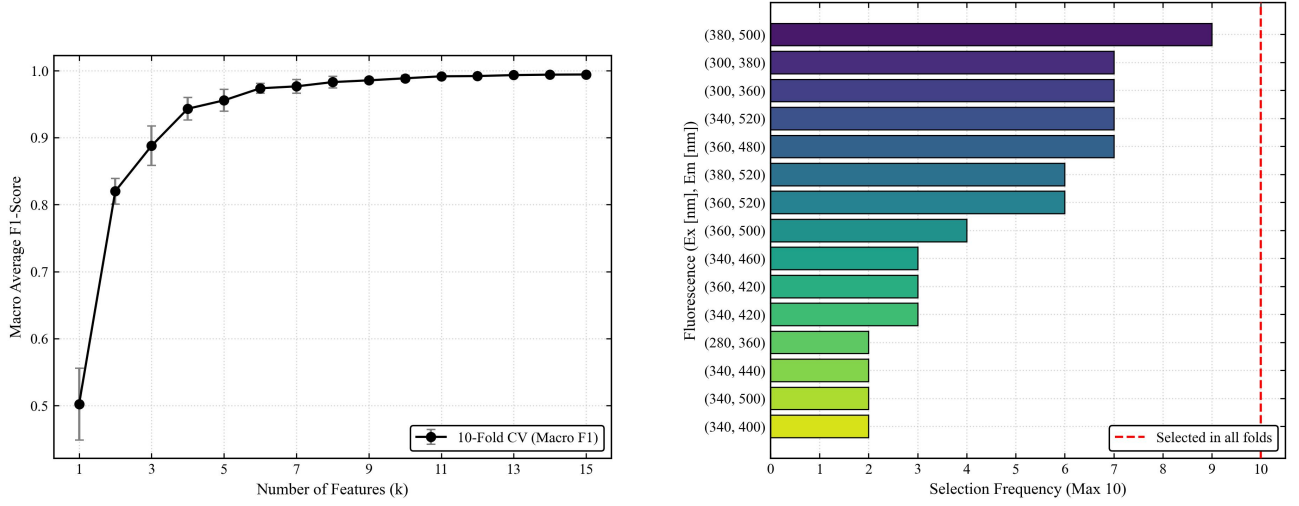
To determine the optimal subset of spectral bands, we implemented a step-wise approach based on the Random Forest Gini Importance described in Section 2.2. The specific procedure is as follows:

1. **Ranking and Stability Analysis:** Instead of a single calculation, we conducted a stability analysis using a 10-fold cross-validation scheme on the calibration set. In each fold, we calculated the feature importance $I_G(X_j)$ and recorded the top-ranked bands. We defined the selection frequency as the number of times a band appeared in the top 10 across the 10 folds. The final ranking was determined based on this frequency to ensure robustness against data variations.
2. **Iterative Evaluation:** We sequentially added spectral bands to the model in descending order of the determined robust ranking. At each step, with the number of features k ranging from 1 to 10, we evaluated the discrimination performance using the Weighted Average F1-Score.
3. **Determination of Optimal Subset:** We adopted the Weighted Average F1-Score of all 9 classes as the evaluation metric. The optimal number of bands k was determined by identifying the point where the accuracy saturated in the internal validation and reached its peak in the external validation. This approach minimizes the number of required images while maximizing the generalization capability.

5. RESULTS

5.1 Optimization of Spectral Bands

Fig. 4(a) shows the results of feature selection by the step-wise method using the calibration dataset. As the number of spectral bands k increased, the Weighted Average F1-Score for all 9 classes rose rapidly, exceeding 0.95 at $k = 5$. The score improvement subsequently plateaued, reaching a saturation level (approx. 0.99) around $k = 11$. Fig. 4(b) shows the selection frequency of each spectral band obtained through 10-fold cross-validation. We observed that the top five bands were selected in more than 7 out of 10 folds.



(a) F1-Score vs. Number of bands k .

(b) Band selection frequency.

Figure 4: Results of the feature selection. (a) Dependence of the Weighted Average F1-Score (y-axis) on the number of spectral bands k (x-axis). Error bars represent standard deviation. (b) Selection frequency (x-axis) of each spectral band (y-axis) during 10-fold cross-validation.

5.2 Generalization Performance on External Validation Set

We validated the generalization capability of the selected subsets using the external validation dataset acquired independently from the calibration dataset. Fig. 5 illustrates the Weighted Average F1-Score on the external set. Contrasting with the internal validation, the performance peaked at $k = 5$ with an F1-score of 0.9171. Notably, this peak score slightly outperformed the baseline score of 0.916 obtained using the full spectrum of 98 bands. Adding features beyond $k = 5$ caused a decrease in accuracy, with the F1-score dropping to 0.880 at $k = 10$. The results indicate that $k = 5$ is the optimal cutoff for this system.

To further investigate how the model distinguishes between polymers, we analyzed the class-wise performance. Fig. 6 presents the F1-score transition for each of the 9 classes, revealing distinct material-dependent behaviors depending on the material type:

- **Early Saturation:** Polymers such as ABS and PVC reached high accuracy exceeding 0.9 with only 1 band. Additionally, PC, PP, and PS demonstrated rapid convergence, reaching their baseline performance levels at $k = 5$.
- **Peak and Drop:** HDPE and PET show a clear peak around $k = 3$ to 5. Notably, for these materials, the F1-scores of the selected subset were higher than the full-spectrum baseline.
- **Slow Saturation:** PMMA and LDPE exhibited a slower convergence to the baseline accuracy compared to other materials.

Fig. 7 presents the confusion matrix obtained with the optimal subset of $k = 5$. The model achieved perfect classification (a recall of 1.00) for ABS, PS, and PVC. In contrast, we observed mutual confusion between PET and HDPE. Specifically, the model misclassified 35% of PET samples as HDPE, and 10% of HDPE samples as PET.

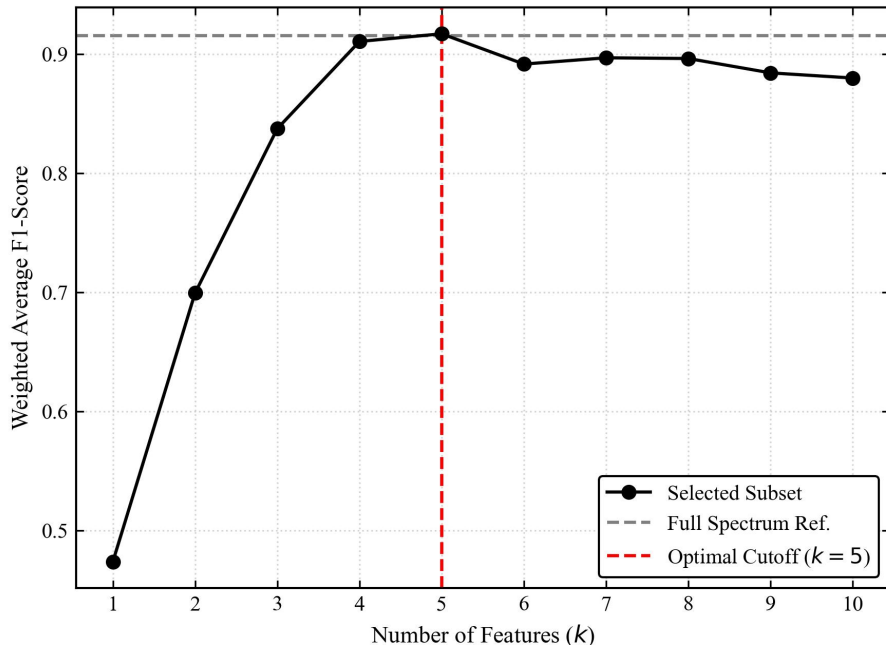


Figure 5: Generalization performance on the external validation dataset. Dependence of the Weighted Average F1-Score (y-axis) on the number of features k (x-axis). The black solid line shows the proposed method, the gray dashed line indicates the full-spectrum baseline (98 bands), and the red dashed line marks the optimal cutoff at $k = 5$.

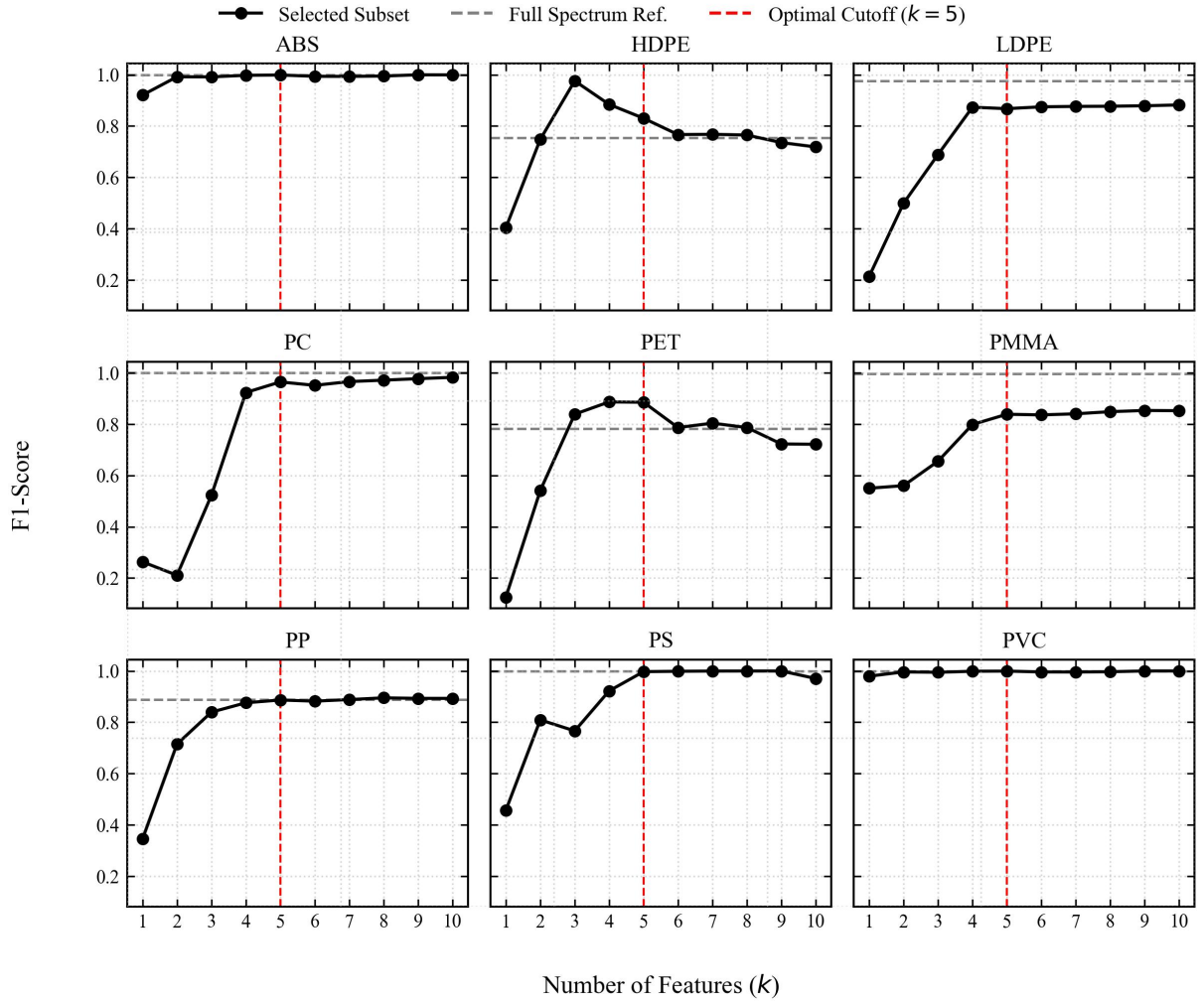


Figure 6: Class-wise classification performance. F1-Score (y-axis) versus the number of features k (x-axis) for each material. The vertical red dashed line indicates the system-wide optimal cutoff ($k = 5$), and the gray dashed line represents the full-spectrum baseline.

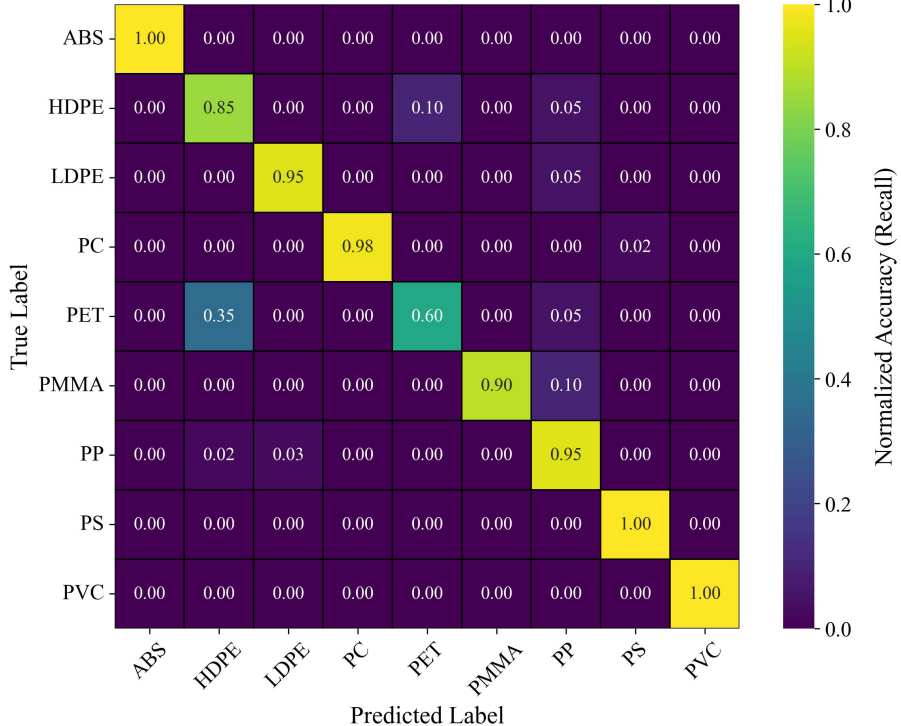


Figure 7: Normalized confusion matrix evaluated on the external validation dataset ($k = 5$). The diagonal elements represent the classification accuracy (Recall) for each class. We observe a distinct confusion between HDPE and PET (True PET is misclassified as HDPE in 35% of cases), highlighting the spectral similarity between these polymers.

6. DISCUSSION

6.1 Interpretation of Optimization Behavior

This study prioritized optimizing the overall average performance for high-throughput screening. The feature selection analysis, as shown in Fig. 4(b), revealed that the top 5 spectral bands were selected in more than 7 out of 10 cross-validation folds, demonstrating the robustness and stability of these features. While including additional bands beyond this optimal subset resulted in a performance decline for specific polymers such as HDPE and PET, the selected 5 bands successfully maximized the system-wide weighted average F1-score. This confirms that identifying a compact and stable feature subset is an effective strategy to ensure generalization capability while minimizing data dimensionality.

6.2 High-Throughput Capability

The primary advantage of this method is the superior throughput achieved by area-scan imaging. While conventional point-scanning methods require time proportional to the number of measurement points, our method acquires spectral information for the entire field of view simultaneously. The experimental results demonstrate a speedup of several orders of magnitude compared to conventional spectroscopic techniques.

6.3 Limitations and Potential Improvements

This study has several limitations. First, as shown in the confusion matrix (Fig. 7), we observed significant confusion between PET and HDPE, with a 35% misclassification rate for PET. While these polymers exhibit distinct spectral fingerprints in the calibration phase, their performance decreased in the external validation. We attribute this to a "distribution shift" between the two datasets, likely caused by subtle variations in lighting geometry and sample orientation during independent measurements. For practical industrial screening, the system must maintain high accuracy regardless of such environmental factors. Therefore, we will focus our future

work on incorporating domain adaptation techniques and expanding the training library to improve the model's robustness against experimental variability. Second, we did not conduct a direct comparison of identification accuracy and measurement time between the proposed method and conventional analytical techniques, such as Fourier Transform Infrared (FTIR) or Raman spectroscopy. Since this study focused on establishing a high-throughput imaging framework using known polymer pellets, a quantitative performance evaluation against these standard methods was not performed in this proof-of-concept stage. Future work will quantify the absolute reliability and processing efficiency of our system by directly comparing its performance with these established point-scanning techniques. Third, the experiments utilized virgin polymer pellets. Since microplastics in actual marine environments may have altered fluorescence characteristics due to biofilm adhesion or weathering, further verification using real environmental samples is necessary.

6.4 System Design for Field Deployment

As a proof-of-principle for high-throughput monitoring, we utilized these findings to design a compact, dedicated system for on-site implementation (Fig. 8). Fig. 8 shows the block diagram of the proposed system. To replace the large benchtop equipment, we adopted high-power UV-LEDs as the light source. However, commercially available LEDs have a wider Full Width at Half Maximum (FWHM) compared to bandpass filters, and the selectable center wavelengths are discrete. This design employs a group of commercially available LEDs that approximately cover the spectral regions identified in the benchtop experiment. In the future, we plan to perform re-optimization of features considering actual hardware characteristics using this compact system. We will adopt a single-board computer (SBC, e.g., Raspberry Pi 5) for control, aiming to realize a low-cost, standalone monitoring solution.

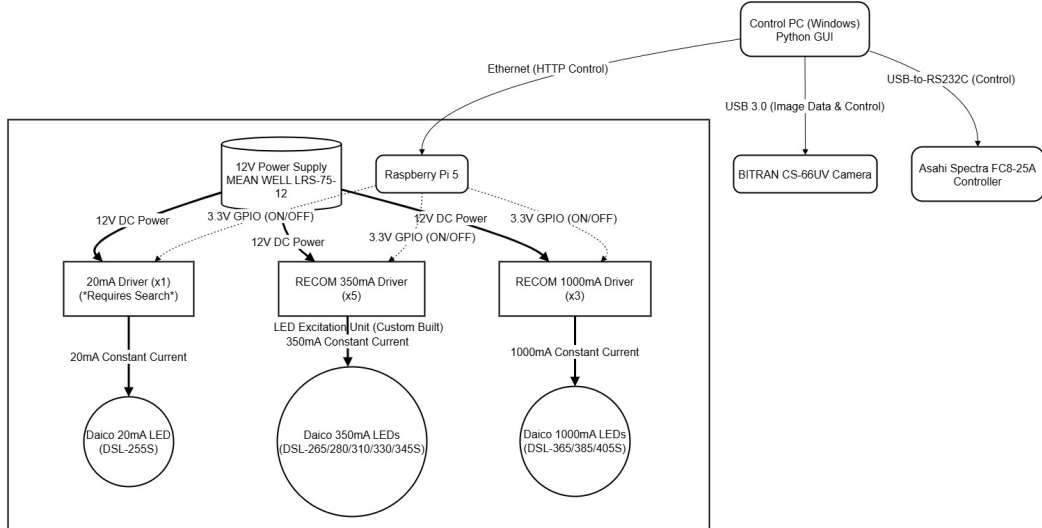


Figure 8: Block diagram of the proposed compact dedicated system. This system uses high-power UV-LEDs and an SBC to achieve a standalone, low-cost solution.

7. CONCLUSION

This study demonstrated the feasibility of a high-throughput microplastic identification method utilizing UV-excited fluorescence imaging. Using a step-wise feature selection approach, we determined that a subset of only five spectral bands yields a weighted F1-score of 0.92 across nine representative plastic types. The proposed method achieves significantly higher throughput compared to conventional point-scanning methods, demonstrating high potential for industrial application. Based on these findings, we also proposed a design for a compact standalone system using UV-LEDs. Feature work will focus on the construction of this dedicated hardware and validation experiments using real marine samples.

REFERENCES

- [1] Hale, R. C., Seeley, M. E., La Guardia, M. J., Mai, L., and Zeng, E. Y., "A global perspective on microplastics," *J. Geophys. Res. Oceans* **125** (Jan. 2020).
- [2] Jambeck, J. R., Geyer, R., Wilcox, C., Siegler, T. R., Perryman, M., Andrade, A., Narayan, R., and Law, K. L., "Marine pollution. plastic waste inputs from land into the ocean," *Science* **347**, 768–771 (Feb. 2015).
- [3] Rocha-Santos, T. and Duarte, A. C., "A critical overview of the analytical approaches to the occurrence, the fate and the behavior of microplastics in the environment," *Trends Analys. Chem.* **65**, 47–53 (Feb. 2015).
- [4] Hidalgo-Ruz, V., Gutow, L., Thompson, R. C., and Thiel, M., "Microplastics in the marine environment: a review of the methods used for identification and quantification," *Environ. Sci. Technol.* **46**, 3060–3075 (Mar. 2012).
- [5] Prata, J. C., da Costa, J. P., Duarte, A. C., and Rocha-Santos, T., "Methods for sampling and detection of microplastics in water and sediment: A critical review," *Trends Analys. Chem.* **110**, 150–159 (Jan. 2019).
- [6] Shim, W. J., Hong, S. H., and Eo, S. E., "Identification methods in microplastic analysis: a review," *Anal. Methods* **9**(9), 1384–1391 (2017).
- [7] Serranti, S., Capobianco, G., Cucuzza, P., and Bonifazi, G., "Efficient microplastic identification by hyperspectral imaging: A comparative study of spatial resolutions, spectral ranges and classification models to define an optimal analytical protocol," *Sci. Total Environ.* **954**, 176630 (Dec. 2024).
- [8] Gebejes, A., Hrovat, B., Semenov, D., Kanyathare, B., Itkonen, T., Keinänen, M., Koistinen, A., Peiponen, K.-E., and Roussey, M., "Hyperspectral imaging for identification of irregular-shaped microplastics in water," *Sci. Total Environ.* **944**, 173811 (Sept. 2024).
- [9] Hall, G. J. and Kenny, J. E., "Estuarine water classification using EEM spectroscopy and PARAFAC-SIMCA," *Anal. Chim. Acta* **581**, 118–124 (Jan. 2007).
- [10] Leavesley, S. J., Walters, M., Lopez, C., Baker, T., Favreau, P. F., Rich, T. C., Rider, P. F., and Boudreaux, C. W., "Hyperspectral imaging fluorescence excitation scanning for colon cancer detection," *J. Biomed. Opt.* **21**, 104003 (Oct. 2016).
- [11] Bui, M. V., Rahman, M. M., Nakazawa, N., Okazaki, E., and Nakauchi, S., "Visualize the quality of frozen fish using fluorescence imaging aided with excitation-emission matrix," *Optics Express* **26**(18), 22954–22964 (2018).
- [12] Rahman, M. M., Shibata, M., Nakazawa, N., Rithu, M. N. A., Nakauchi, S., Hagiwara, T., Osako, K., and Okazaki, E., "Non-destructive approach for the prediction of pH in frozen fish meat using fluorescence fingerprints in tandem with chemometrics," *G.* **7**, 364 (Nov. 2022).
- [13] Maes, T., Jessop, R., Wellner, N., Haupt, K., and Mayes, A. G., "A rapid-screening approach to detect and quantify microplastics based on fluorescent tagging with nile red," *Sci. Rep.* **7**, 44501 (Mar. 2017).
- [14] Li, S., Zhu, Y., Li, Y., and Lam, E. Y., "Fluorescence polarimetry for microplastics identification," in *Holography, Diffractive Optics, and Applications XV*, Zhou, C., Cao, L., Poon, T.-C., and Yoshikawa, H., eds., 53, SPIE (Nov. 2025).
- [15] Hassoun, A., Sahar, A., Lakhal, L., and Aït-Kaddour, A., "Fluorescence spectroscopy as a rapid and non-destructive method for monitoring quality and authenticity of fish and meat products: Impact of different preservation conditions," *Lebenson. Wiss. Technol.* **103**, 279–292 (Apr. 2019).
- [16] Dankowska, A. and Kowalewski, W., "Comparison of different classification methods for analyzing fluorescence spectra to characterize type and freshness of olive oils," *Eur. Food Res. Technol.* **245**, 745–752 (Mar. 2019).
- [17] Gorji, H. T., Shahabi, S. M., Sharma, A., Tande, L. Q., Husarik, K., Qin, J., Chan, D. E., Baek, I., Kim, M. S., MacKinnon, N., Morrow, J., Sokolov, S., Akhbardeh, A., Vasefi, F., and Tavakolian, K., "Combining deep learning and fluorescence imaging to automatically identify fecal contamination on meat carcasses," *Sci. Rep.* **12**, 2392 (Feb. 2022).
- [18] Bolton, F. J., Bernat, A. S., Bar-Am, K., Levitz, D., and Jacques, S., "Portable, low-cost multispectral imaging system: design, development, validation, and utilization," *J. Biomed. Opt.* **23**, 1–11 (Dec. 2018).
- [19] Mathews, S. A., "Design and fabrication of a low-cost, multispectral imaging system," *Appl. Opt.* **47**, F71–6 (Oct. 2008).

- [20] Beck, E. A., Lefcourt, A. M., Lo, Y. M., and Kim, M. S., “Use of a portable fluorescence imaging device to facilitate cleaning of deli slicers,” *Food Control* **51**, 256–262 (May 2015).
- [21] Jeon, S., Lee, J., Beak, K., Park, B., and Kang, H., “Analysis of microplastic types and sizes using a fluorescence-based optical system,” *Current Optics and Photonics* **9**(4), 418–426 (2025).
- [22] Chatterjee, D. P., Pakhira, M., and Nandi, A. K., “Fluorescence in “nonfluorescent” polymers,” *ACS Omega* **5**, 30747–30766 (Dec. 2020).
- [23] Lakowicz, J. R., “Instrumentation for fluorescence spectroscopy,” in [*Principles of Fluorescence Spectroscopy*], 27–61, Springer US, Boston, MA (2006).